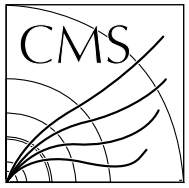

The Compact Muon Solenoid Experiment

CMS Note

Mailing address: CMS CERN, CH-1211 GENEVA 23, Switzerland

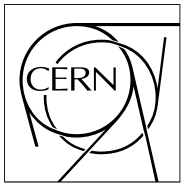

11 June 2006

Search for the heavy neutral MSSM Higgs bosons with the H/A$\rightarrow \tau^+\tau^- \rightarrow$ electron + jet decay mode

R. Kinnunen and S. Lehti

Helsinki Institute of Physics, Helsinki, Finland

Abstract

Prospects of finding the heavy neutral MSSM Higgs bosons A and H with the H/A$\rightarrow \tau^+\tau^-$ decay mode and electron+jet final state in the associated production with b quarks in $\mathrm{gg} \rightarrow \mathrm{bbH/A}$ are studied in CMS at the LHC collider. Full simulation and reconstruction of the CMS detector at the luminosity of $2\times10^{33}\mathrm{cm}^{-2}\mathrm{s}^{-1}$ is used.

1 Introduction

In the Minimal Supersymmetric extension of the Standard Model (MSSM) two Higgs doublets are required to preserve the supersymmetry. The physical Higgs states are the two CP-even Higgs bosons h and H, a CP-odd Higgs boson A and two charged Higgs bosons $H^{\pm}$. Due to the $\tan^2\beta$ enhancement of the couplings to down type fermions, with respect to the Standard Model (SM), the $A/H \to b\bar{b}$ and $A/H \to \tau^+\tau^-$ decay modes dominate and the production is mainly through the associated production process $gg \to b\bar{b}H/A$ at large $\tan\beta$ region ($\gtrsim$ 10). The $A/H \to \tau^+\tau^-$ decays can be searched for in several final states: two leptons, muon+jet, electron+jet and two jets [1] . Several fast and partially full simulation studies [2],[3], [4] have shown that the large $\tan\beta$ ($\gtrsim$ 10) region can be covered with at least one final state and the value of $\tan\beta$ could be measured with good precision from event rates [3]. The main SM background from $Z/\gamma^* \to \tau^+\tau^-$ can be efficiently suppressed by tagging the associated b jet(s). In this work the electron+jet final states are studied with full simulation and reconstruction of the CMS detector at the luminosity of $2\times10^{33}\mathrm{cm}^{-2}\mathrm{s}^{-1}$.

The general MSSM is assumed taking for the model parameters the following values: M_2 = 200 GeV/c^2, μ = 200 GeV/c^2, M_3 = 800 GeV/c^2, M_{SUSY} = 1 TeV/c^2. The results are presented in the maximal mixing scenario fixing X_t ($X_t = A_t - \mu\cot\beta$) to 2 TeV/c^2. The top mass is set to 175 GeV/c^2. The choice of SUSY parameters can affect the production rate through the branching fraction and through SUSY loop corrections in the production cross section. The SUSY-loop corrections have been calculated recently and are shown to be particularly sensitive to the magnitude and the sign of the higgsino mass parameter μ [5]. Large positive (negative) μ values can lead to a reduction (enhancement) of of the cross section.

The LEP and the Tevatron colliders have performed direct searches for heavy neutral Higgs bosons. The LEP measurements yield lower bounds of 91.0 and 91.9 GeV/c^2 for h and A mass in MSSM, respectively [6]. The excluded $\tan\beta$ regions are 0.5< $\tan\beta$ < 2.4 for the maximal m_h scenario and 0.7< $\tan\beta$ < 10.5 for the no-stop-mixing scenario with m_{top} = 175 GeV/c^2 [6].

The production cross sections and branching ratios are discussed in Section 2 and the simulation of events in Section 3. The event selection methods are explained in Section 4 and the signal-to-background ratios are given in Section 5. Uncertainties of the background estimation are discussed in Section 6. The statistical significance and the discovery potential are given in Section 7 and the conclusions in Section 8.

2 Phenomenology

2.1 Production and decay

The most important processes for the production of the neutral MSSM Higgs boson at the LHC are the gluon fusion $gg \to H/A$ and Higgs boson strahlung off b quarks $gg \to b\bar{b}H/A$. For small and moderate values of $\tan\beta$ ($\lesssim$ 10) the loop-mediated gluon fusion has more importance, but at large $\tan\beta$ the associated production dominates, representing about 90% of the total cross section. The next-to-leading order (NLO) cross sections for the h, H and A bosons in the associated production process are shown in Fig. 1 as a function of m_A with $\tan\beta$ = 20. The cross sections are calculated with the FeynHiggs program [7]. The production cross sections for the H and A bosons are almost equal at large m_A, but for $m_A < m_h^{max}$ (m_H^{min}) the H production decreases rapidly while the production cross section for h increases to the same order as that for A. The CP-even Higgs bosons h and H are also produced in the weak gauge boson fusion $qq \to qqH$, but the cross sections are sizeable only near the upper (lower) mass bound of h and H, where these Higgs bosons are SM-like.

Figure 2 shows the $H \to \tau^+\tau^-$ branching fraction for m_H = 140 and 500 GeV/c^2 and for μ = $\pm$ 200 and $\pm$ 500 GeV/c^2 as a function of $\tan\beta$ calculated with FeynHiggs [7]. Sensitivity to the μ parameter increases with increasing $\tan\beta$ and is larger for larger absolute values of this parameter. The enhancement with positive μ values could partly cancel the expected large negative contributions from the SUSY loop corrections for these μ values. The NLO cross sections times branching fractions are shown in Table 1 for m_A = 130-500 GeV/c^2. For the two lowest mass points, m_A = 130 and 140 GeV/c^2, the mass of the lighter scalar Higgs boson h is only 4.4 and 11.2 GeV/c^2 smaller than m_A. With the mass resolution, which can be reached in the $H \to \tau^+\tau^-$ decay channels, the lighter scalar contributes to the signal and is added in the cross sections for m_A = 130 and 140 GeV/c^2 in Table 1. The contribution is 31 and 11% of the total production rate, respectively.

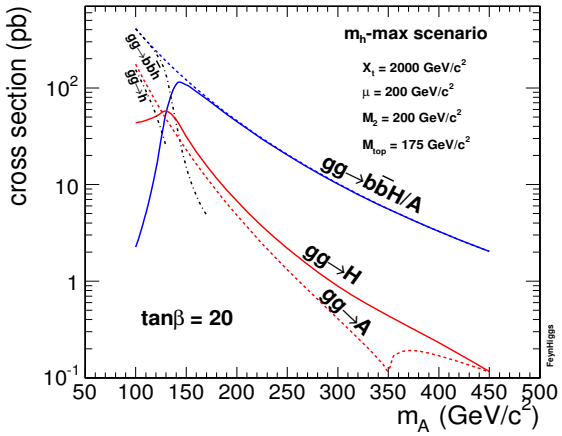

Figure 1: Production cross sections for the heavy neutral MSSM Higgs bosons H (solid lines) and A (dashed lines) and for the lighter scalar Higgs boson h (dash-dotted lines) in the associated production $gg \to b\bar{b}h/H/A$ and in the gluon-gluon fusion $gg \to h/H/A$ with $\tan\beta = 20$ as a function of m_A.

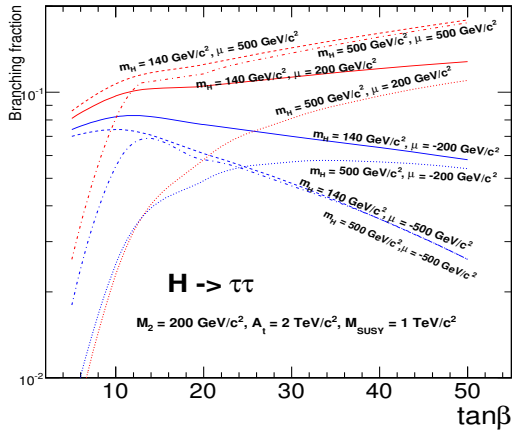

Figure 2: Branching fraction for $H \to \tau^+\tau^-$ with $m_H = 140$ and 500 GeV/c^2 as a function of $\tan\beta$ for $\mu = \pm 200$ GeV/c^2 (solid lines) and for $\mu = \pm 500$ GeV/c^2 (dashed lines).

		$\sigma \times$ BR (pb)
$b\bar{b}H/A/h, H/A/h \to \tau^+\tau^- \to e + \tau$-jet + X	$m_A = 130$ GeV/c^2, $\tan\beta = 20$	18.2
$b\bar{b}H/A/h, H/A/h \to \tau^+\tau^- \to e + \tau$-jet + X	$m_A = 140$ GeV/c^2, $\tan\beta = 20$	12.8
$b\bar{b}H/A, H/A \to \tau^+\tau^- \to e + \tau$-jet + X	$m_A = 200$ GeV/c^2, $\tan\beta = 20$	4.15
$b\bar{b}H/A, H/A \to \tau^+\tau^- \to e + \tau$-jet + X	$m_A = 300$ GeV/c^2, $\tan\beta = 20$	0.85
$b\bar{b}H/A, H/A \to \tau^+\tau^- \to e + \tau$-jet + X	$m_A = 500$ GeV/c^2, $\tan\beta = 20$	0.071
$Z/\gamma^* \to \tau^+\tau^- \to e + \tau$-jet + X	$90 < m_{\tau\tau} < 300$GeV/c^2	331.81
$Z/\gamma^* \to \tau^+\tau^- \to e + \tau$-jet + X	$m_{\tau\tau} > 300$GeV/c^2	0.1407
$b\bar{b}Z/\gamma^*, Z/\gamma^* \to \tau^+\tau^-$	$60 < m_{\tau\tau} < 100$GeV/c^2	26.0
$b\bar{b}Z/\gamma^*, Z/\gamma^* \to \tau^+\tau^-$	$m_{\tau\tau} > 100$GeV/c^2	1.0
$t\bar{t}$		840
$W\bar{t}$		6.16
W+jet, $W \to e\nu_e$	$p_T^{jet} > 80$GeV/c	1890.0
$Z/\gamma^*, Z/\gamma^* \to e^+e^-$	$5 < m_{e^+e^-} < 150$GeV/c^2	810.8
$b\bar{b}Z/\gamma^*, Z/\gamma^* \to e^+e^-$		26.3

Table 1: Cross section times branching fraction for the signal and background processes. Preselection efficiencies are not included.

2.2 Background processes

The signal process $gg \to bbH/A$, $H/A \to \tau^+\tau^-$, $\tau_1 \to e\nu_e\nu_\tau$, $\tau_2 \to$ hadrons $+ \nu_\tau$ leads to a final state of one isolated electron, an isolated τ jet and one or two detectable b jets. The background with genuine τ's comes from two types of processes, Z/γ^* events decaying into $\tau\tau$, and the $t\bar{t}$ and Wt events, where the $e + \tau$ jet final state can come from direct W decays to an electron and a τ or through $W \to \tau\nu_\tau \to e + \nu_e\nu_\tau\nu_\tau$ decays. The inclusive production of Z/γ^* and the production in association of $b\bar{b}$ are considered separately:

- $Z/\gamma^* \to \tau^+\tau^- \to e + \tau$ jet + X
- $b\bar{b}Z/\gamma^*, Z/\gamma^* \to \tau^+\tau^- \to e + \tau$ jet + X
- $t\bar{t}$ with one $W \to \tau\nu_\tau$, the other $W \to e\nu_e\nu_\tau$ or $W \to \tau\nu \to e\nu_e\nu_\tau$
- Wt, with one $W \to \tau\nu_\tau$, the other $W \to e\nu_e\nu_\tau$ or $W \to \tau\nu \to e\nu_e\nu_\tau$

Background can arise also from the processes where a hadronic jet or an electron leads to a fake τ:

- $\mathrm{t\bar{t}}$ with $\mathrm{W_1} \to \mathrm{qq'}$, $\mathrm{W_2} \to \mathrm{e}\nu_\mathrm{e}\nu_\tau$ or $\mathrm{W_2} \to \tau\nu \to \mathrm{e}\nu_\mathrm{e}\nu_\tau$
- Wt, with $\mathrm{W_1} \to \mathrm{qq'}$, $\mathrm{W_2} \to \mathrm{e}\nu_\mathrm{e}\nu_\tau$ or $\mathrm{W_2} \to \tau\nu \to \mathrm{e}\nu_\mathrm{e}\nu_\tau$
- W+jet, with $\mathrm{W} \to \mathrm{e}\nu_\mathrm{e}$
- $\mathrm{Z}/\gamma^* \to \mathrm{e^+e^-}$
- $\mathrm{b\bar{b}Z}/\gamma^*, \mathrm{Z}/\gamma^* \to \mathrm{e^+e^-}$

The NLO production cross sections for these processes are shown in Table 1. Preselections are applied on the $\mathrm{Z}/\gamma^* \to \tau^+\tau^-$, W+jet and $\mathrm{Z}/\gamma^* \to \mathrm{e^+e^-}$ backgrounds. For the $\mathrm{Z}/\gamma^* \to \tau^+\tau^-$ and W+jet backgrounds, the cuts $\mathrm{p_T} > 10$ GeV/c and $|\eta| < 2.4$ have been applied on the electron from one of the τ's and on the electron from the W. For the $\mathrm{Z}/\gamma^* \to \mathrm{e^+e^-}$ background, these cuts were applied on both electrons. For this background, the electrons through τ decays were excluded. The QCD multi-jet events present a large potential background, through hadronic jets faking both the electron and the τ jet, and is considered in this work.

3 Simulation and reconstruction

The signal events were generated with PYTHIA [8] for five Higgs boson masses 130, 140, 200, 300 and 500 GeV/c^2. The TAUOLA package [9] was used for simulating τ decays. The signal cross sections and branching fractions were calculated with FeynHiggs [7] in the $\mathrm{m_h}$-max scenario.

The Z/γ^* background associated with light quark and gluon jets was generated with PYTHIA [8]. A NLO cross section of 1437 pb [10] calculated with the program MCFM [11] assuming $\tau^+\tau^-$ final state and $\mathrm{m_{\tau^+\tau^-}} > 90$ GeV/c^2 was used. The background consisting of Z/γ^* events produced in association with b quarks emitted mostly in the forward direction was generated with CompHEP [12]. For these backgrounds cross sections were calculated with CompHEP. The leading-order (LO) cross section for $\tau^+\tau^-$ final state is 26 pb. No $\mathrm{p_T}$ or η cuts were applied on b quarks in the $\mathrm{b\bar{b}Z}/\gamma^*$ process generation. The b quarks were assumed to have nonzero mass. To avoid double counting, the $\mathrm{b\bar{b}Z}/\gamma^*$ events are removed from the inclusive the Z/γ^* samples in the beginning of the analysis. The inclusive $\mathrm{t\bar{t}}$ events were generated with PYTHIA, and and single top (tW) events with TopREX [13]. Cross sections of 840 pb and 60 pb were used for $\mathrm{t\bar{t}}$ and tW events, respectively. The W+jet background was generated with PYTHIA. For the QCD multi-jet background largest contribution can be expected from the $\hat{\mathrm{p}}_\mathrm{T}$ interval above the $\mathrm{E_T}$ threshold for the τ jet. Events generated with $50 < \hat{\mathrm{p}}_\mathrm{T} < 80$ GeV were used for the determination of the τ selection efficiency. Due to limited Monte-Carlo (MC) statistics no trigger simulation was performed on this sample.

The reconstruction was based on CMS digitized data sets. For the data sets used in this work, the response of the CMS detector was simulated with the CMSIM [14] and OSCAR [15] packages including a pile-up corresponding to the luminosity of $2\times10^{33}\mathrm{cm^{-2}s^{-1}}$. The physics objects were reconstructed with the standard methods available in the CMS reconstruction software. Version ORCA_8_7_4 of the CMS OO Reconstruction [16] was used. The primary vertex was reconstructed and selected with an algorithm searching for the highest sum of the transverse momenta of the associated tracks. Jets were reconstructed in a cone of 0.5 and the jet energies were calibrated with correction factors obtained from MC studies [17]. In the correction method, $\mathrm{E_T}$ thresholds were set on the Electromagnetic calorimeter (ECAL) cells (0.8 GeV) and and on the Hadron calorimeter (HCAL) cells (0.5 GeV). The missing transverse energy ($\mathrm{E_T^{miss}}$) was reconstructed from the full calorimeter response summing the ECAL-plus-HCAL towers. For this measurement the hadronic jet energies were calibrated with correction factors obtained from a simulation of QCD photon+jet events [17]. These corrections were applied on jets with $\mathrm{E_T} > 20$ GeV. A regional track reconstruction method of reconstructing tracks around the lepton and jet directions was used.

4 Event selection

4.1 Trigger

The events were triggered with a single electron trigger and with an electron-plus-τ jet trigger (eTau trigger) [18, 19]. The combined eTau trigger requires the presence of both an electron and a τ-jet, with thresholds lower than those used for single electron and single τ triggers. The τ-jet candidate at Level-1 is defined as the most energetic τ-jet, which is not collinear with the electron candidate. The τ identification takes advantage of the properties of hadronic τ decay, narrowness of the energy deposition in the calorimeter at the Level-1 and isolation

of the narrow jet at the High Level Trigger (HLT). The Level-1 E_T threshold was taken to be 40 GeV for the τ jet and 19 GeV/c for the electron. Energy corrections, derived from Monte-Carlo data, were applied on the reconstructed Level-1 τ jet. Tables 2 and 3 show the Level-1 trigger efficiencies for the signal and background events, respectively.

The selection of electrons in the High-Level Trigger (HLT) for single electron trigger proceeds in three steps. The first step uses the calorimeter information alone. The next step demands hits in the pixel detectors consistent with an electron candidate. In the final step the selection of electrons uses full track reconstruction seeded from the pixel hits obtained by the matching step. The trigger threshold for single electrons is 26 GeV/c.

At the HLT, the identification of τ jets begins with the reconstruction of a jet in a region centered on the Level-1 τ jet. The electromagnetic calorimeter is used for the isolation of the τ jet candidate summing the energies of the ECAL cells in a cone of $0.13 < \Delta R < 0.4$ around the Level-1 τ jet and demanding the energy sum to be below 5 GeV. The identification of a τ jet with charged particle tracks is also based on isolation criteria. The tracks were reconstructed in the pixel detector around the Level-1 τ-jet direction. The track with maximum p_T is searched for in a cone of 0.1 around the jet direction. A small cone with $\Delta R = 0.07$ around the leading track is taken as a signal cone requiring this signal cone to be isolated in a larger cone of $\Delta R = 0.4$ counting all pixel tracks in this area. The cut $p_T > 3$ GeV/c, is applied on the leading track. At this level, no requirement is made on the number of tracks in the signal cone, to keep one- and three-prong τ decays.

The efficiencies for the Level-1 selection, and for the HLT selection for single electron plus eTau trigger are shown in Tables 2 and 3. The numbers for the total efficiency include the preselection efficiencies. The efficiency for the Wt background is affected with the forcing of W and top decays.

4.2 Offline reconstruction

4.2.1 Electron identification

The reconstructed electrons were first required to be isolated in the tracker demanding that no track with $p_T > 1$ GeV/c was found in a cone of $\Delta R = 0.4$ around the electron direction. Figure 3 shows the p_T distribution for all reconstructed and isolated electron candidates. Agreement of the isolated electron spectrum with the spectrum of the generated electron from $\tau \to e\nu_\tau\nu_e$ is satisfactory already at this level at large p_T^e ($\gtrsim$ 40 GeV). A small fraction of events with $p_T^e(MC) \sim 0$ is triggered with an electron or an electron-type object from other sources than $\tau \to e\nu_\tau\nu_e$. For a fraction of these events the $\tau \to e\nu_\tau\nu_e$ decay was found but the p_T of the generated electron was small ($p_T^e(MC) \lesssim$ 2 GeV/c). On the average $\sim$ 1.3 reconstructed electron candidates were found in the signal events. The electron identification was performed with variables described in Ref.[20], exploiting hadronic cluster energy over the electromagnetic energy ($E^{hadronic}/E^{em}$), sum of the 3×3 energy matrix over the sum of the 5×5 energy matrix centered on the the crystal with largest E_T ($E(3\times3)/E(5\times5)$), second order moment of the η projection of the shower transversal profile ($\sigma_{\eta\eta}$), supercluster energy (E^{sc}) over the track momentum (E^{sc}/p^{track}), differences between the reconstructed supercluster η and ϕ positions with respect to the track position ($\Delta\eta$ and $\Delta\phi$) and the variable $|1/E^{sc} - 1/p^{track}|$. Figure 4 shows the distributions of these variables for the genuine electrons from $\tau \to e\nu_\tau\nu_e$ and for the leading hadronic track from $\tau \to \text{hadrons} + \nu_\tau$ for the signal events with m_A = 200 GeV/c^2. The cut values used in the following, the cut efficiencies and the purity for each cut are shown in Table 4. The largest improvement to the purity is due to the $E^{hadronic}/E^{em}$ and E^{sc}/p^{track} cuts. The p_T spectrum for the isolated electrons passing the identification cuts is shown in Fig. 3. The efficiency for an electron candidate to pass the selection is 64.2%, including the tracker isolation. The fraction of signal events where at least one identified electron is found is 81.2%.

4.2.2 Identification of τ jet

To preserve the $\tau \to \pi^\pm + n\pi^0 + \nu_\tau$ decays modes, presenting a fraction of 52% of all hadronic τ decays, a τ identification method based on calorimeter jet reconstruction was used. The τ-jet candidates were reconstructed in

Table 2: Efficiencies of the Level-1 and HLT triggers for the signal events with m_A = 130-500 GeV/c^2 and tanβ = 20.

m_A (GeV/c^2)	130	140	200	300	500
Level-1	72.2%	75.6%	85.5%	92.9%	96.7%
HLT	11.6%	12.9%	18.1%	23.2%	29.8%
Total efficiency	8.4%	9.8%	15.4%	21.6%	28.8%

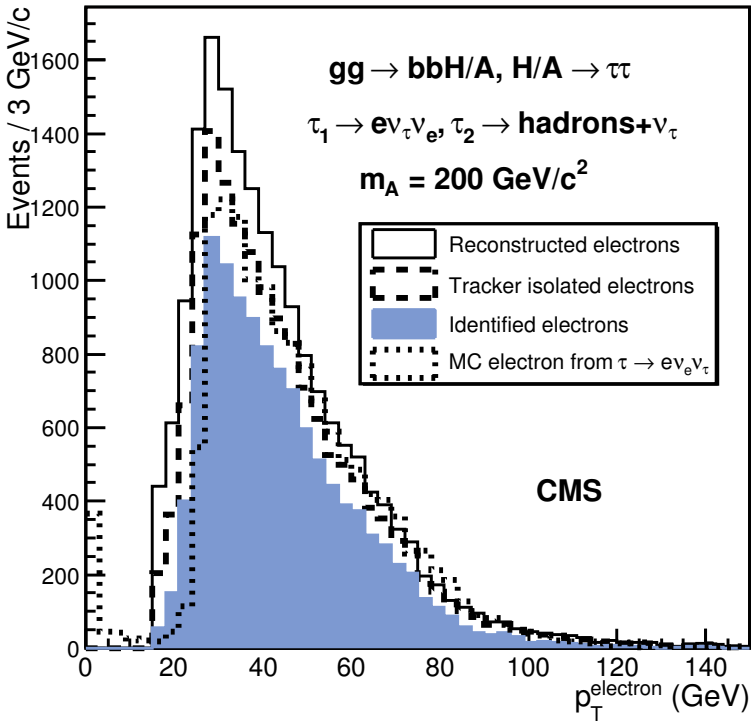

Figure 3: Distribution of p_T for all reconstructed (solid line) electron candidates, for isolated electron candidates (dashed line), for identified electrons (filled histogram) and for generated electrons from $\tau \to e\nu_\tau\nu_e$ (dotted line) for $gg \to b\bar{b}H/A$, $H/A \to \tau^+\tau^- \to e + \tau$ jet + X with $m_A = 200$ GeV/c^2 and tan$\beta = 20$.

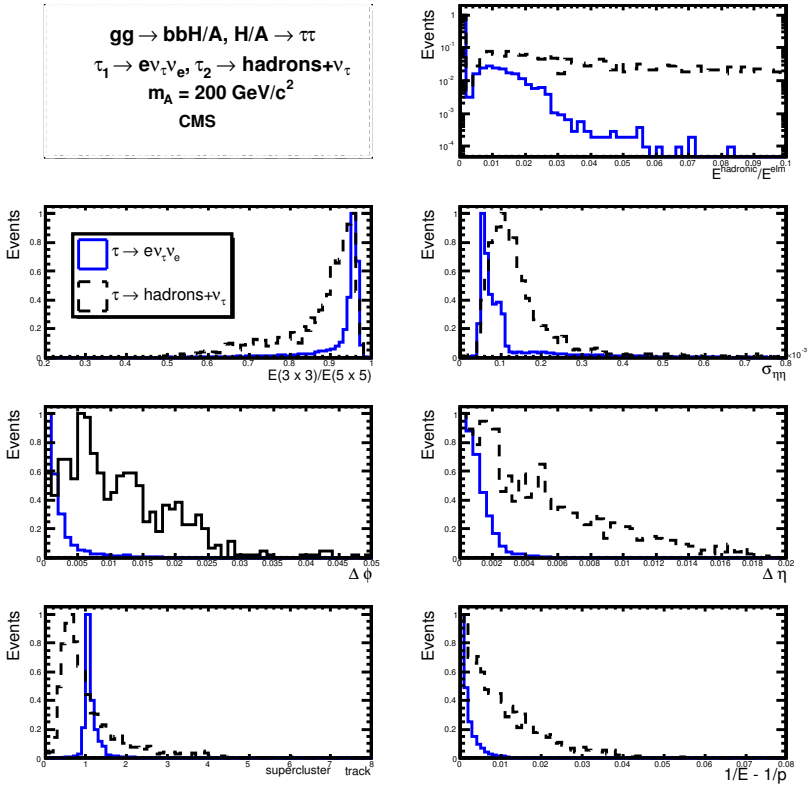

Figure 4: Distributions of electron identification variables for the electron from $\tau \to e\nu_\tau\nu_e$ (solid line) and for the leading charged hadron from $\tau \to$ hadrons + ν_τ in the $gg \to b\bar{b}H/A$, $H/A \to \tau^+\tau^- \to e + \tau$ jet + X events with $m_A = 200$ GeV/c^2 and tan$\beta = 20$.

	Preselection	Level-1	HLT	Total efficiency
$Z/\gamma^* \to \tau^+\tau^-$	0.414	44.8%	28.0%	5.2%
$b\bar{b}Z/\gamma^*, Z/\gamma^* \to \tau^+\tau^-$		60.7%	5.2%	3.1%
$t\bar{t}$		96.3%	11.7%	11.3%
Wt		94.7%	34.7%	32.8%
W+jet	0.468	89.3%	51.8%	21.6%
$Z/\gamma^* \to e^+e^-$	0.429	96.6%	78.5%	32.5%
$b\bar{b}Z/\gamma^*, Z/\gamma^* \to e^+e^-$		90.6%	73.6%	66.7%

Table 3: Efficiencies of the preselection, Level-1 trigger and the HLT triggers for the background events.

the calorimeter in a cone of 0.4. Jet energy corrections evaluated for one- and three-prong τ decays were used. The identified electron was removed from the sample of τ-jet candidates. Figure 5 shows the E_T of the reconstructed τ jet over the E_T of the MC τ jet for the signal events with m_A = 200 GeV/c^2, indicating a well measured τ-jet energy scale. The offline E_T cut on the τ jet was taken to be $E_T^{jet} > 40$ GeV. At this level the electron contamination from $\tau^\pm \to e\nu_e\nu_\tau$ is 0.9%.

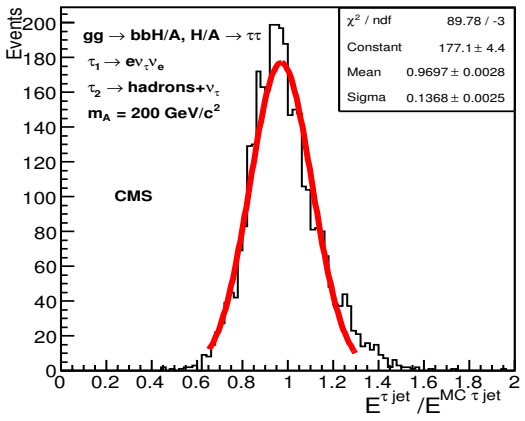

Figure 5: Ratio of the reconstructed and generated E_T for the identified τ jet for the signal events with m_A = 200 GeV/c^2 and tanβ = 20.

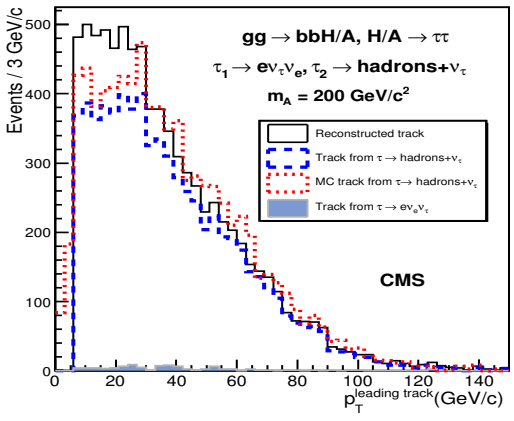

Figure 6: Distribution of p_T for the leading track in the τ jet for the signal events with m_A = 200 GeV/c^2 and tanβ = 20.

The tracks were reconstructed inside the jet reconstruction cone. The leading track (trk1) was searched for in a cone of $\Delta R = 0.1$ around the τ-jet direction. For an efficient isolation against the hadronic jets a small signal cone is necessary and was taken to be $\Delta r = 0.04$. The fraction of three-prong τ jets is 26% at this level. The distribution of reconstructed tracks with $p_T > 1$ GeV/c in the signal cone into one to five prongs is shown in Table 5 for one - and three-prong τ decays for $E_T^{\tau jet} > 40$ GeV. About 83% of the $\tau^\pm \to \text{hadron}^\pm + n\pi^0 + \nu_\tau$ decays are reconstructed as one prong τ's. The large fraction of two-prong τ jets from the $\tau^\pm \to 3\ \text{hadrons}^\pm + n\pi^0 + \nu_\tau$

m_A (GeV/c^2)	Efficiency	Purity
Tracker isolation	83.6%	91.7%
$E^{hadronic}/E^{elm} < 0.02$	87.3%	96.1%
$E(3\times3)/E(5\times5) < 0.75$	95.3%	96.3%
$\sigma_{\eta\eta} < 0.0004$	96.8%	96.3%
$\Delta\phi < 0.015$	99.5%	96.5%
$\Delta\eta < 0.005$	99.2%	96.8%
$E^{sc}/p^{track} > 0.8$	97.3%	97.2%
$\lvert 1/E^{sc} - 1/p^{track}\rvert < 0.015$	99.4%	97.5%
Total efficiency	62.6%	97.5%

Table 4: Electron identification efficiency and purity for $gg \to b\bar{b}H/A$, $H/A \to \tau^+\tau^-$, $\tau_1 \to \ell\nu_\tau\nu_e$, $\tau_2 \to$ hadrons $+ \nu_\tau$ with m_A = 200 GeV/c^2 and tanβ = 20.

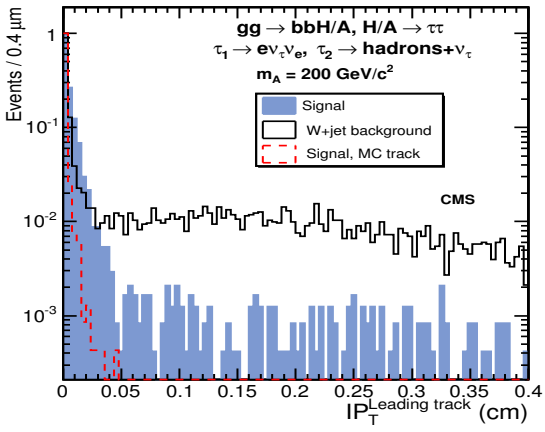

Figure 7: Distribution of the transverse impact parameter for the leading track with $p_T^{track} > 20$ GeV for the signal events with m_A = 200 GeV/c^2 (shaded area), for the the W+jet events (solid line) and for the MC track in the signal events (dashed line).

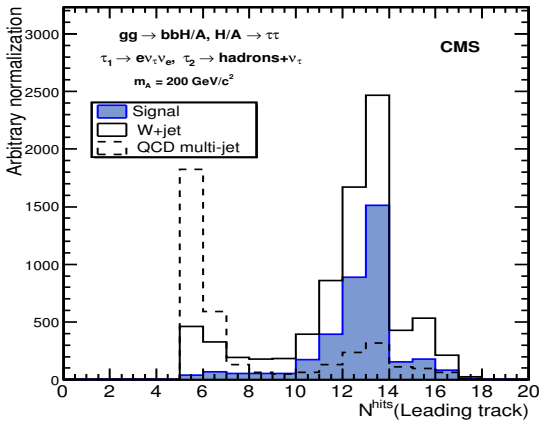

Figure 8: Distribution of hits in the full silicon tracker for the leading track with all τ selection cuts, including the impact parameter cut, for the signal events with m_A = 200 GeV/c^2 (shaded histogram), for the W+jet events (solid line) and for the QCD multi-jet events (dashed line).

Table 5: Distribution of reconstructed tracks with $p_T > 1$ GeV/c in the signal cone $\Delta R = 0.04$ for one- and three-prong τ decays in the signal events with m_A = 200 GeV/c^2.

Reconstructed tracks	1	2	3	4	≥5
$\tau^{\pm} \to \text{hadron}^{\pm} + n\pi^0 + \nu_\tau$	82.8%	10.2%	4.2%	1.6%	1.1%
$\tau^{\pm} \to 3\ \text{hadrons}^{\pm} + n\pi^0 + \nu_\tau$	14.4%	35.6%	44.6%	3.9	1.8%

decays is due to the narrow signal cone selected.

Figure 6 shows the p_T distribution of the leading track in the τ-jet candidates with the $E_T^{jet} > 40$ GeV for the signal events with m_A = 200 GeV/c^2. The distributions for the reconstructed tracks and for the MC tracks from $\tau^{\pm} \to \text{hadron}^{\pm} + n\pi^0 + \nu_\tau$ are also shown in the figure. For a small fraction of events ($\sim 1\%$) the leading track is an electron from $\tau^{\pm} \to e\nu_e\nu_\tau$. Requirement of an energetic leading track is one of the handles to disentangle the τ jets from the hadronic jets. To guarantee an efficient rejection against the QCD multi-jet events, $p_T^{trk1} > 20$ GeV/c was selected. In addition to the leading track, two other tracks were accepted in the signal cone to account for the $\tau^{\pm} \to 3\ \text{hadrons}^{\pm} + n\pi^0 + \nu_\tau$ decays.

The isolation was performed counting tracks with $p_T > 1$ GeV/c in the area between the signal cone (0.04) and the isolation cone, which was taken to be then same as the jet reconstruction cone $\Delta R = 0.4$. The efficiencies are shown in Table 6 for the signal with m_A = 130 - 500 GeV/c^2 and and in Table 7 for the background processes.

Accidental track reconstruction problems, like shared hits, can lead to a fake large-p_T tracks in the hadronic jets, as has been shown in Ref.[21]. These fake leading tracks may appear in the W + jet and hadronic multi-jet events. As was proposed in Ref.[21], the fake tracks can be suppressed with an upper bound in the transverse impact parameter of the leading track and with a requirement of at least eight hits in the full silicon tracker. Figure 7 shows the distribution of the transverse impact parameter for the leading track with $p_T > 20$ GeV/c and $E_T^{jet} > 40$ GeV in the signal events with m_A = 200 GeV/c^2 and in the W+jet events with the requirement of eight hits. Efficiencies for the cut $IP_T < 0.3$ mm are shown in Tables 6 and 7. The fake τ jets from W+jet are suppressed by a factor of four. Figure 8 shows the number of reconstruction hits for the leading track with $p_T > 20$ GeV/c in the full silicon tracker for the signal events with m_A = 200 GeV/c^2 and for the W+jet and QCD multi-jet backgrounds, with all selection cuts including the impact parameter cut. The tracks in the signal events show a good quality with $\gtrsim$ 10 hits. The W+jet and multi-jet backgrounds are further suppressed by factors of 1.3 and 3, respectively, when at least eight hits are required.

The $Z/\gamma^* \to e^+e^-$ and $b\bar{b}Z/\gamma^*, Z/\gamma^* \to e^+e^-$ backgrounds contain an isolated genuine electron to pass the

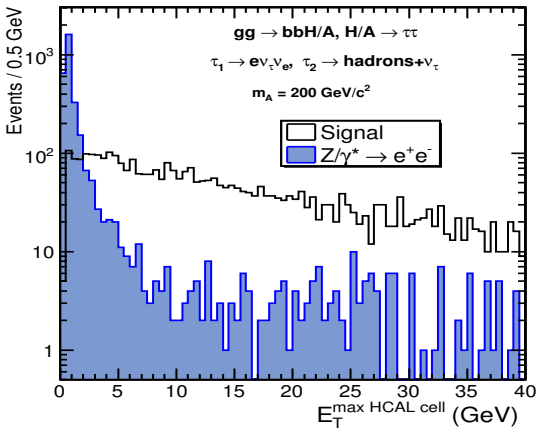

Figure 9: Distribution of E_T of the most energetic HCAL cell in the τ jet for the signal with m_A = 200 GeV/c^2 and tanβ = 20 (solid line) and for the $Z/\gamma^* \to e^+e^-$ background (filled histogram).

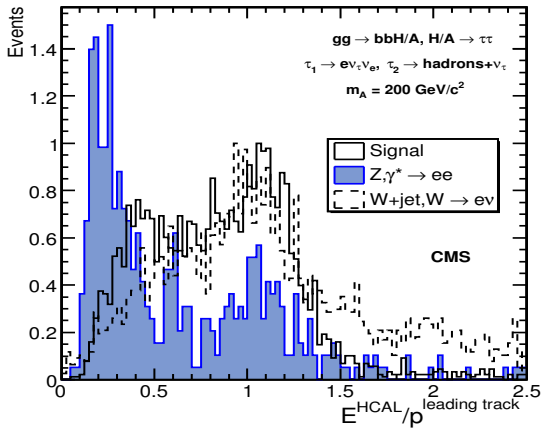

Figure 10: Ratio of the HCAL energy to the momentum of the leading track in the τ jet for the signal events with m_A = 200 GeV/c^2 and tanβ = 20 (solid line), for the τ candidates in the $Z/\gamma^* \to e^+e^-$ (filled histogram) and W+jet (dashed line) backgrounds.

Table 6: Efficiencies (%) for the offline τ selection cuts and τ-selection purity for events passing the trigger, primary vertex reconstruction and the electron identification cuts for the signal events with m_A = 130-500 GeV/c^2 and tanβ = 20.

m_A (GeV/c^2)	130	140	200	300	500
$E_T^{jet} > 40$ GeV	62.2	65.4	79.0	86.1	89.5
$p_T^{trk1} > 20$ GeV/c	62.5	64.3	70.5	74.5	80.9
1 or 3 signal tracks	72.9	76.1	79.6	82.6	82.4
Tracker isolation	67.6	68.6	72.5	73.9	74.5
$IP_T^{trk1} < 0.03$ mm	91.8	93.2	94.6	96.0	93.0
$N_{hits}^{trk1} \geq 8$	96.2	96.1	95.3	94.9	96.3
$E_T^{max} > 2$ GeV	95.4	95.3	96.4	97.1	97.6
$0.35 < E^{HCAL}/p^{trk1} < 1.5$	89.6	90.1	89.7	88.3	88.3
τ-selection efficiency	14.2	16.9	24.8	30.6	34.3
τ-selection purity	97.8	98.2	97.0	95.6	96.0

electron cuts and are not significantly suppressed with the τ selection cuts as can be seen from Table 7. These electronic τ-candidates can be suppressed requiring a large energy deposition in the hadron calorimeter. Figure 9 shows the E_T of the most energetic HCAL cell (E_T^{max}) in the τ jet for the signal and for the $Z/\gamma^* \to e^+e^-$ background. The cut $E_T^{max} > 2$ GeV suppresses the electrons with a factor of ~ 7. A further reduction can be obtained comparing the HCAL and track measurements. Figure 10 shows the HCAL energy in the τ jet over the momentum of the leading track (E^{HCAL}/p^{trk1}) in the one-prong τ jets for the signal events with m_A = 200 GeV/c^2 compared to the same ratio in the $Z/\gamma^* \to e^+e^-$ and W+jet events, including the cut $E_T^{max} > 2$ GeV. The cut $E^{HCAL}/p^{trk1} > 0.35$, applied on the one-prong τ candidates only, suppresses further the electronic τ candidates by a factor of ~ 1.8. The W+jet events show a tail at large values of E^{HCAL}/p^{trk1} due to the neutral hadron component of the hadronic jets. An upper bound of 1.5 suppresses the hadronic jets by $\sim 15\%$.

The τ-jet identification cuts, described above, yield a good purity of $\sim 97\%$ for the signal events. The contamination from the electrons from $\tau \to e\nu_\tau\nu_e$ is reduced to $\sim 0.4\%$. A rejection factor of ~ 600 is obtained for the hadronic jets in the QCD multi-jet events generated with $50 < \hat{p}_T < 80$ GeV/c. The charges of the identified electron and τ jet are required to be opposite summing the charges of the tracks for the three-prong τ jets.

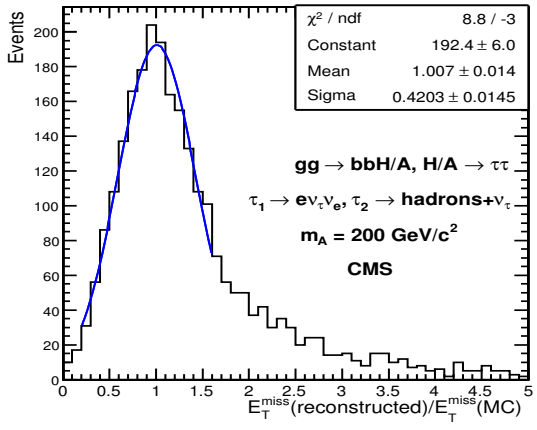

Figure 11: Ratio of the reconstructed and generated missing transverse energy for the signal events with m_A = 200 GeV/c^2 and tanβ = 20.

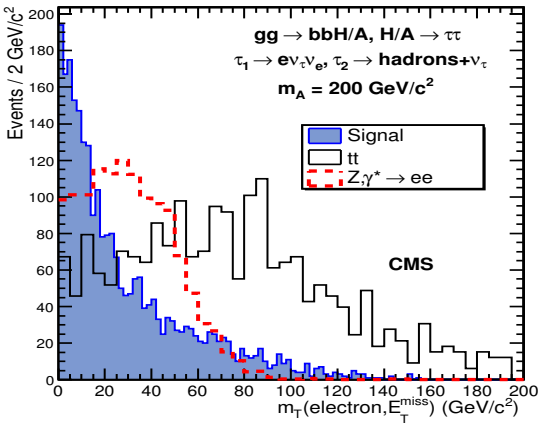

Figure 12: Distribution of transverse mass reconstructed from the electron and the missing transverse energy for the signal with m_A = 200 GeV/c^2 and tanβ = 20 (filled histogram), for the $t\bar{t}$ (solid line) and for the $Z/\gamma^* \to e^+e^-$ (dashed line) background. Histogram normalization is arbitrary.

Table 7: Efficiencies (%) of the offline τ selection cuts on the τ-jet candidates after removing the identified electron for the background events passing the trigger, primary vertex reconstruction and electron identification cuts. No trigger simulation and electron reconstruction was used for the QCD multi-jet background.

	$Z\gamma^*\tau\tau$	$b\bar{b}Z\tau\tau$	$t\bar{t}$	Wt	W+jet	$Z\gamma^*$ee	$b\bar{b}Z\gamma^*$ee	QCD
$E_T^{jet} > 40$ GeV	32.3	53.1	75.1	69.9	88.4	60.4	56.8	50.4
$p_T^{trk1} > 20$ GeV/c	87.4	49.7	49.8	51.6	60.5	72.8	70.3	42.1
1 or 3 signal tracks	62.5	66.3	58.1	68.8	53.5	91.8	89.4	39.8
Tracker isolation	38.5	33.3	21.9	39.4	19.9	62.9	54.6	21.9
IP_T^{track} <0.03 mm	84.0	74.3	23.5	78.5	13.7	96.6	93.9	58.0
$N_{hits}^{trk1} \geq 8$	80.0	72.4	80.8	84.3	81.5	65.9	66.2	30.9
$E_T^{max} > 2$ GeV	94.6	88.5	69.8	61.6	98.7	16.9	19.1	95.6
$0.35 < E^{HCAL}/p^{trk1} < 1.5$	89.9	87.0	79.4	83.0	85.1	54.1	51.7	85.1
τ selection efficiency	3.9	2.4	0.5	3.1	0.5	1.5	1.2	0.27

4.3 Missing transverse energy

Figure 11 shows the ratio of the reconstructed and the generated missing transverse energy for the signal events with m_A = 200 GeV/c^2. Due to the small E_T^{miss} from neutrinos in the signal events, the resolution is modest and a tail from large fluctuations is visible.

The E_T^{miss} measurement can be exploited to suppress the $t\bar{t}$ background with an upper bound in the transverse mass $m_T(e, E_T^{miss})$ reconstructed from the electron and the missing transverse energy. Figure 12 shows the $m_T(e, E_T^{miss})$ distribution for the signal events with m_A = 200 GeV/c^2 and for the W+jet and $Z/\gamma^* \to e^+e^-$ backgrounds with the electron and τ-jet selections. In this variable the backgrounds with $W \to e\nu_e$ decays are distributed close to the W mass while the signal is distributed at small $m_T(e, E_T^{miss})$ values because for the signal the missing transverse energy is due to the neutrinos originating from the τ's. An upper bound $m_T(e, E_T^{miss}) < 40$ GeV/c^2 reduces the W+jet background with a factor of ~ 4 and retains 74% of the signal. The shape of the distribution for the $Z/\gamma^* \to e^+e^-$ background is due to the random distribution of the fake missing transverse energy.

4.4 Tagging of b jets and veto on additional central jets

The event selection was continued for the events where at least one hadronic jet with $E_T^{jet} > 20$ GeV was found. A probabilistic secondary vertex algorithm with a discriminator cut from Ref. [22] was used for b tagging. The cut in

the discriminator was set to 0.8, which suppresses efficiently the Z/γ^*, W+jet and the QCD multi-jet background. The efficiency to tag at least one hadronic jet in the signal events was found to be 32% for m_A = 200 GeV/c^2 excluding the jet finding efficiency. The efficiency in the inclusive Z/γ^* samples and for the W+jet events was found to be below 3%. The efficiencies including the jet finding efficiency are between 13 and 19% for the signal with m_A = 130-500 GeV/c^2, below 1% for the Z/γ^* backgrounds and 1.3% for the W+jet background. The larger efficiency for the W+jet background with respect to the Z/γ^* backgrounds is due to the $b\bar{b}W$ component present in the W+jet sample, while for the Z/γ^* backgrounds the $b\bar{b}Z/\gamma^*$ component was generated separately. The purity is high (99%) in the signal events.

The $t\bar{t}$ background, with a genuine electron, τ and b jets, cannot be significantly suppressed with the cuts described above. This background, however, can be suppressed with a veto on the remaining central jets, after tagging one jet. The additional jets with $E_T > 20$ GeV were searched for in the region $|\eta| < 2.5$. Fake jets, which generally do not contain tracks, were suppressed with a cut in the variable defined as the sum of the track p_T values over the jet E_T,

$$\alpha = \Sigma p_T^{track}/E_T^{jet}. \quad (1)$$

The cut $\alpha > 0.1$ was found to improve the veto efficiency for the signal by about 10%. The veto efficiency is around 60% for the signal samples and $\sim 5\%$ for the $t\bar{t}$ background.

4.5 Higgs boson mass reconstruction

The neutrinos from the τ's in the $H/A \to \tau^+\tau^-$ decays are emitted close to the directions of the measured τ decay products allowing the Higgs boson mass to be reconstructed. The neutrino energies were estimated by dividing the missing energy between the neutrino directions, which is possible when the two τ's are not in a back-to-back configuration. Events with these configurations were removed with an upper bound in the $\Delta\varphi(\tau_1, \tau_2)$ between the τ jet and the electron in the transverse plane. Uncertainties of the missing energy measurement can lead to negative neutrino energies. About 40% of the signal events were lost when positive neutrino energies were required. This requirement, however, yields a further suppression of the $t\bar{t}$, tW and W+jet backgrounds, since for these backgrounds the neutrinos are generally not emitted along the true or fake τ's. The efficiencies of the $E_{\nu_1} > 0$ and $E_{\nu_2} > 0$ cuts for these backgrounds are around 40%. Figures 13, 14 and 15 show the reconstructed Higgs boson mass distributions for the signal events with m_A = 130, 200 and 300 GeV/c^2. The mass resolutions from the Gaussian part of the fit are 16, 22 and 21%, respectively.

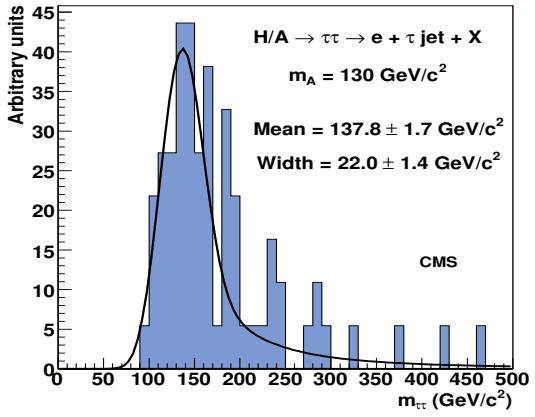

Figure 13: Reconstructed Higgs boson mass for m_A = 130 GeV/c^2 and tanβ = 20.

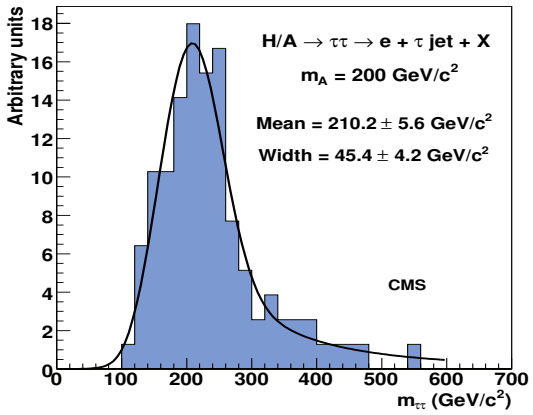

Figure 14: Reconstructed Higgs boson mass for m_A = 200 GeV/c^2 and tanβ = 20.

5 Results

The event selection cuts described in the previous sections are summarized below:

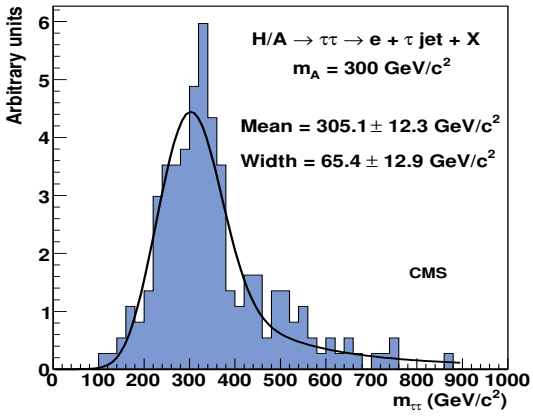

Figure 15: Reconstructed Higgs boson mass for the signal with m_A = 300 GeV/c^2 and tanβ = 20.

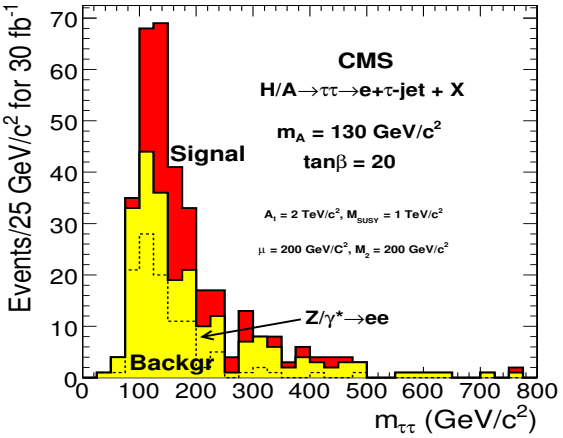

Figure 16: Reconstructed Higgs boson mass for the signal with m_A = 130 GeV/c^2 and tanβ = 20 and for the total background for an integrated luminosity of 30 fb^{-1}. The dashed line shows the sum of the $Z/\gamma^* \rightarrow e^+e^-$ and $b\bar{b}Z/\gamma^*, Z/\gamma^* \rightarrow e^+e^-$ backgrounds.

1. Identified isolated electron, $p_T > 20$ GeV/c, $|\eta| < 2.5$
2. One identified τ jet:
   - Calorimeter jet with $E_T > 40$ GeV and $|\eta| < 2.5$
   - Leading track with $p_T > 20$ GeV/c in the τ jet within ΔR <0.1 around the calorimeter jet direction
   - No tracks with $p_T > 1$ GeV/c in the cone $0.04 < \Delta R < 0.4$ surrounding the leading track direction
   - One or three tracks with $p_T > 1$ GeV/c in the signal cone $\Delta r < 0.04$
   - $IP_T < 0.3$ mm and at least eight hits for the leading track
   - $E_T^{max} > 2$ GeV and $0.35 < E^{HCAL}/p^{trk1} < 1.5$
3. $Q^{\tau\ jet} \times Q^e$ = -1
4. Transverse mass cut: $m_T(e, E_T^{miss}) < 40$ GeV/c^2

Table 8: Higgs boson mass, production cross sections times branching fraction, efficiencies (%) for the selection cuts and numbers of events for 30 fb^{-1} for the signal with tanβ = 20.

m_A (GeV/c^2)	130	140	200	300	500
$\sigma \times$ BR (pb)	18.2	14.4	4.15	0.83	0.071
trigger	1.53 (8.4)	1.41 (9.8)	0.640 (15.4)	0.180 (21.6)	0.0204 (28.8)
primary vertex	1.44 (94.1)	1.33 (94.4)	0.603 (94.2)	0.175 (97.2)	0.0191 (91.4)
electron id.	1.11 (77.8)	1.04 (78.8)	0.484 (80.8)	0.137 (73.7)	0.0141 (73.8)
one id. τ-jet	0.128 (11.4)	0.142 (13.7)	0.113 (23.4)	4.52×10^{-2}(41.7)	5.88×10^{-3}(41.7)
$Q^{\tau jet} \times Q^e$=-1	0.128 (100.0)	0.141 (99.3)	0.112 (99.1)	4.49×10^{-2}(99.3)	5.82×10^{-3}(99.0)
m_T <40 GeV/c^2	9.85×10^{-2}(77.6)	0.106 (75.2)	8.25×10^{-2}(73.7)	3.11×10^{-2}(69.3)	3.88×10^{-3} (66.7)
$\geq$1 jet	4.51×10^{-2}(45.9)	4.52×10^{-2}(42.8)	3.84×10^{-2}(46.6)	1.51×10^{-2} (48.6)	2.07×10^{-3}(53.5)
b tagging	1.34×10^{-2}(29.7)	1.44×10^{-2}(31.9)	1.16×10^{-2}(30.2)	4.97×10^{-3}(32.9)	7.57×10^{-4}(36.5)
jet veto	8.06×10^{-3}(60.2)	8.54×10^{-3}(59.3)	7.24×10^{-2}(62.4)	3.14×10^{-3}(63.2)	4.62×10^{-3}(61.0)
$\Delta\varphi_{\tau\tau} < 175^o$	7.64×10^{-3}(94.8)	7.96×10^{-3}(93.2)	6.81×10^{-3}(94.1)	2.69×10^{-3}(85.7)	3.44×10^{-3}(74.5)
$E_{\nu_1,\nu_2} > 0$	4.13×10^{-3}(54.1)	4.71×10^{-3}(59.2)	4.20×10^{-3}(61.7)	1.73×10^{-3}(64.3)	2.43×10^{-3}(70.6)
N_{events}	93.0	106.2	92.4	51.9	7.3

Table 9: Background process, production cross sections times branching fraction, cross sections and efficiencies (%) for the selection cuts and number of events for 30 fb^{-1} .

	$Z/\gamma^* \to \tau^+\tau^-$	$b\bar{b}Z/\gamma^* \to \tau^+\tau^-$	$Z/\gamma^* \to e^+e^-$	$b\bar{b}Z/\gamma^* e^+e^-$
$\sigma \times$ BR (pb)	331.8	27.0	1890	26.3
preselection	173.5 (41.4)		811.2 (42.9)	
trigger	17.3 (10.0)	0.818 (3.1)	617.4 (76.1)	18.2 (67.2)
primary vertex	16.5 (95.4)	0.796 (97.3)	591.9 (95.9)	17.7 (97.3)
double count. on Z/γ^*	15.6 (94.6)	0.796 (100.0)	561.8 (94.9)	17.7 (100.0)
electron identification	11.6 (74.4)	0.585 (80.2)	281.4 (50.1)	9.31 (52.6)
one identified τ-jet	0.134 (1.2)	1.0×10^{-2} (1.8)	3.40 (1.2)	9.00×10^{-2} (1.0)
$Q^{\tau\ \mathrm{jet}} \times Q^e$ = -1	0.129 (96.3)	1.0×10^{-2} (100)	3.31 (97.4)	8.80×10^{-2} (97.8)
m_T <40 GeV/c^2	9.84×10^{-2} (76.3)	8.0×10^{-3} (80.0)	2.26 (68.3)	5.50×10^{-2} (62.5)
$\geq$1 jet, $E_T > 20$ GeV	3.99×10^{-2} (40.6)	5.6×10^{-3} (70.0)	0.85 (37.6)	2.98×10^{-2} (54.2)
b tagging	1.35×10^{-3} (1.1)	2.6×10^{-3} (46.4)	1.51×10^{-2} (1.8)	9.60×10^{-3} (32.2)
jet veto	5.70 $\times10^{-4}$ (42.2)	1.5×10^{-3} (57.7)	6.04×10^{-3} (41.4	5.90×10^{-3} (67.4)
$\Delta\varphi(\tau_1,\tau_2) < 175^o$	4.90 $\times10^{-4}$ (86.0)	1.36×10^{-3} (90.7)	4.83×10^{-3} (80.0)	5.06×10^{-3} (85.7)
$E_{\nu_1,\nu_2} > 0$	1.97 $\times10^{-4}$ (40.2)	7.60×10^{-4} (55.9)	1.71×10^{-4} (39.0)	1.93×10^{-3} (50.0)
Number of events	5.9	22.8	51.3	57.9

Table 10: Background process, production cross sections times branching fraction, cross sections and efficiencies (%) for the selection cuts and number of events for 30 fb^{-1} .

	$t\bar{t}$	Wt	W+jet
$\sigma \times$ BR (pb)	840	6.16	673.2
preselection			315.0 (46.8)
trigger	94.4 (11.3)	2.00 (32.5)	145.6 (46.2)
primary vertex	93.9 (99.5)	1.97 (98.5)	143.9 (98.8)
electron identification	66.7 (71.0)	1.43 (72.6)	114.2 (79.4)
one id. τ-jet	0.636 (0.95)	4.10×10^{-2} (2.87)	0.567 (0.5)
$Q^{\tau\ \mathrm{jet}} \times Q^e$ = -1	0.571 (89.8)	4.00×10^{-2} (97.6)	0.469 (82.7)
$m_T(e, E_T^{miss})$ <40 GeV/c^2	0.139 (24.3)	8.0×10^{-3} (20.0)	0.118 (25.2)
$\geq$1 jet, $E_T > 20$ GeV	0.137 (98.6)	6.9×10^{-3}(86.3)	5.45×10^{-2} (46.2)
b tagging	9.40×10^{-2} (68.6)	4.1×10^{-3} (59.4)	1.58×10^{-3} (2.9)
jet veto	5.10×10^{-3} (5.4)	2.38×10^{-3}(58.1)	6.62×10^{-4} (41.9)
$\Delta\varphi_{\tau\tau} < 175^o$	4.92×10^{-3} (96.4)	2.33×10^{-3} (98.0)	5.56×10^{-4} (83.9)
$E_{\nu_1,\nu_2} > 0$	2.01 $\times10^{-3}$ (40.9)	9.60×10^{-4} (41.2)	2.14×10^{-4} (38.5)
Number of events	60.3	28.8	6.4

5. One tagged b-jet with $E_T > 20$ GeV, discriminator > 0.8
6. Veto on additional jets with $E_T > 20$ GeV and $|\eta| < 2.5$
7. Higgs boson mass reconstruction
   - $\Delta\varphi(\tau_1,\tau_2) < 175^0$
   - $E_{\nu_1,\nu_2} > 0$

Table 8 shows the numbers of events for 30 fb^{-1} and the efficiency for all the event selection cuts described above for the signal events with m_A = 130-500 GeV/c^2 and tanβ = 20. The cross section times branching fraction, trigger efficiency and the efficiency of the primary vertex reconstruction are also shown in the tables. Table 9 shows the number of events and efficiencies for the backgrounds originating from $Z/\gamma^* \to \tau^+\tau^-$ and $Z/\gamma^* \to e^+e^-$ decays in the inclusive and in the associated $b\bar{b}Z/\gamma^*$ production. The efficiency of removing the $b\bar{b}Z/\gamma^*$ component from the inclusive Z/γ^* samples is also shown. Table 10 shows the same for the backgrounds involving W's from $t\bar{t}$, Wt and W+jet events. The mass windows were selected to optimize the significance. The backgrounds in the selected mass windows and the total background for the five Higgs boson masses are shown in Table 11.

Due to the insufficient MC statistics, factorization was used to estimate the hadronic multi-jet background. The τ-identification efficiency was estimated from QCD multi-jet events generated with $50 < \hat{p}_T < 80$ GeV/c. This $\hat{p}_T$

Table 11: Number of background events for 30 fb^{-1} in the mass windows selected for m_A = 130, 140, 200, 300 and 500 GeV/c^2.

mass window (GeV/c^2)	120-200	130-220	140-280	240-480	360-780
$Z/\gamma^* \to \tau^+\tau^-$	2.8	0.9	0.9	0.4	0.2
$b\bar{b}Z/\gamma^* \to \tau^+\tau^-$	6.9	6.9	7.9	2.3	0.4
$Z/\gamma^* \to e^+e^-$	20.3	17.1	18.1	3.5	1.7
$b\bar{b}Z/\gamma^* e^+e^-$	26.7	21.8	20.8	8.7	1.5
$t\bar{t}$	15.0	15.0	16.0	15.8	13.9
Wt	8.8	10.9	13.9	6.0	2.7
W+jet	2.1	3.1	5.1	2.3	1.6
Total background	82.6	75.7	82.7	39.0	22.0

interval can be expected to give the largest contribution to the hadronic jet background. The τ selection efficiency of 2.7×10^{-3} was found for the jets in this sample. Due to the strong isolation cuts used this efficiency can be expected to remain at the same level for $\hat{p}_T > 80$ GeV/c. For the estimation of the absolute background the events were assumed to be triggered with the single electron trigger with $p_T > 26$ GeV/c. The alternative τ-jet trigger, based also on isolations and E_T threshold, can be expected to lead to similar result. The hadronic jets can pass the electron trigger through the $\pi^\pm/\pi^0$ overlap, π^0 conversions and semileptonic b and c decays. The background rate from these sources is 9×10^7 events in a year corresponding to the integrated luminosity of 20 fb^{-1}, as estimated in Ref. [19]. The electron identification efficiency on the hadronic jets passing the electron trigger is 0.1 according to Refs. [23],[24],[25]. Tagging of one b jet yields another important reduction of the hadronic jet background. To account for the heavy flavors in the QCD multi-jet events, the result obtained for the W+jet background containing the $b\bar{b}W$ component was used. This efficiency is 5.7×10^{-3} including the efficiency for a veto on additional jets. Due to the presence of fake E_T^{miss} only, the efficiency of the $m_T(e, E_T^{miss})$ cut can be assumed to be the same as for the $Z/\gamma^* \to e^+e^-$ events. Efficiencies of charge correlation and Higgs boson mass reconstruction were taken to be 50%, according to Ref. [26], where genuine QCD multi-jet samples have been studied for the $H/A \to \tau^+\tau^- \to 2jet + X$ signal. The efficiency of the mass window cut was also taken from the same reference scaled to mass window used in this work around m_A = 200 GeV/c^2. These factors are summarized in Table 12 and yield a a total rejection factor of 1.6×10^7 for the QCD multi-jet events passing the electron trigger. The background expected for 30 fb^{-1} is 8.4 events in the mass window around m_A = 200 GeV/c^2.

Table 12: Efficiency of the selection cuts for the QCD multi-jet background passing the single electron trigger.

Off-line electron identification	0.1
Off-line τ jet identification	2.7×10^{-3}
b tagging and jet veto, from W+jet events	5.7×10^{-3}
$Q^{\tau\ jet} \times Q^e$ = -1, from Ref. [26]	0.5
$m_T(e, E_T^{miss}) < 40$ GeV/c^2 from $Z/\gamma^* \to e^+e^-$ events	0.7
$\Delta\varphi(\tau_1, \tau_2) < 175^0$, from $Z/\gamma^* \to e^+e^-$ events	0.8
$E_{\nu_1,\nu_2} > 0$, from Ref. [26]	0.5
Mass window cut, scaled from Ref. [26]	0.3
Total efficiency	6.5×10^{-8}

Figures 16, 17 and 18 show the reconstructed Higgs boson mass distributions of the $H/A \to \tau^+\tau^- \to$ electron + jet + X signal and the total background for 30 fb^{-1} with m_A = 130 GeV/c^2, tanβ = 20, m_A = 200 GeV/c^2, tanβ = 20 and m_A = 300 GeV/c^2, tanβ = 25. The sum of the $Z/\gamma^* \to e^+e^-$ and $b\bar{b}Z/\gamma^*$, $Z/\gamma^* \to e^+e^-$ backgrounds is shown separately in the figures.

6 Systematic uncertainty on background determination

The uncertainty of the event selection efficiency is related to the uncertainty of the electron and τ identification, the absolute calorimeter scale and b tagging efficiency. The systematic uncertainty due to the energy scale was estimated varying the jet energy and the E_T^{miss} values with the expected energy scale uncertainties yielding an average 5.1% uncertainty on the number of Z/γ^* events, 3.8% uncertainty on the number of $b\bar{b}Z/\gamma^*$ events, 7.3% uncertainty on the number of $t\bar{t}$ events, 11.3% uncertainty on the number of tW events and 11.8% uncertainty on the number of W+jet events passing the event selection cuts. The uncertainty of the b tagging can be estimated from $t\bar{t}$ events as in Ref. [27]. A value of 5% is used as a conservative estimate. The mistagging uncertainty is also

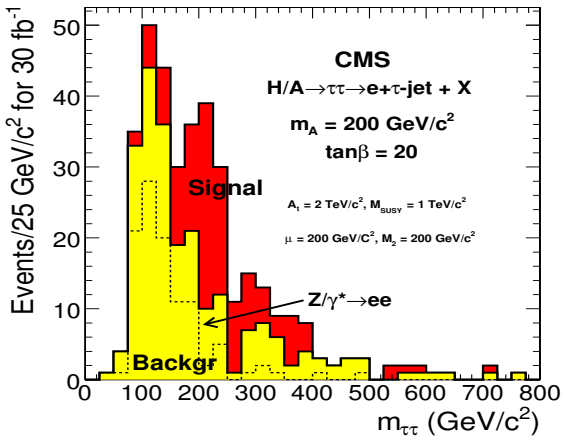

Figure 17: Reconstructed Higgs boson mass for the signal with m_A = 200 GeV/c^2 and tanβ = 20 and for the total background for an integrated lumonosity of 30 fb^{-1}. The dashed line shows the sum of the $Z/\gamma^* \rightarrow e^+e^-$ and $b\bar{b}Z/\gamma^*, Z/\gamma^* \rightarrow e^+e^-$ backgrounds.

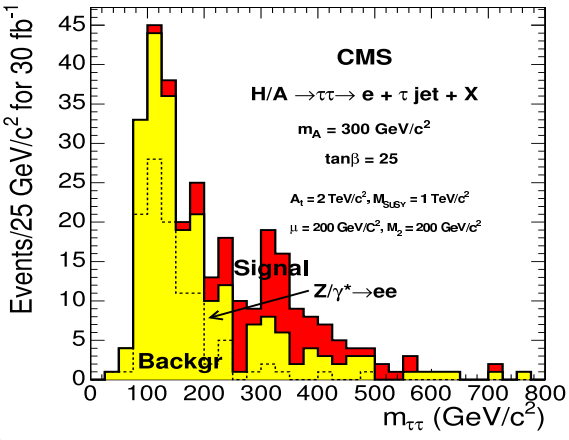

Figure 18: Reconstructed Higgs boson mass for the signal with m_A = 300 GeV/c^2 and tanβ = 25 and for the total background for an integrated lumonosity of 30 fb^{-1}. The dashed line shows the sum of the $Z/\gamma^* \rightarrow e^+e^-$ and $b\bar{b}Z/\gamma^*, Z/\gamma^* \rightarrow e^+e^-$ backgrounds.

assumed to be 5%. An electron identification uncertainty of 2% is used.

The background level under the signal peak could be obtained with fits to the background determining the position of the Z peak from the Z/γ^* background without b tagging. In this work a Monte-Carlo method was used with theoretical cross section uncertainties or expected experimental uncertainties to be measured combining the results several processes. The uncertainty of the $b\bar{b}Z/\gamma^*$ cross section measurement from data has been studied in Ref. [28] and found to be 14.2%, excluding the luminosity uncertainty. The uncertainty of the Z/γ^* cross section is expected to be of the order of 1% from theoretical studies [29]. For the $t\bar{t}$ background the theoretical NLO cross section uncertainty derives from the scale uncertainty, taken to be 5% according to Ref. [27], and the PDF uncertainty, $\sim$ 2.5 %, yielding 5.6 % for the total uncertainty. The same uncertainty is used for the cross sections of the tW and W+jet processes. With these estimates, the total systematic uncertainty, including the luminosity uncertainty of 3%[17], was found to be 8.1%, 15.9%, 11.1%, 14.0% and 14.5% for the Z/γ^*, $b\bar{b}Z/\gamma^*$, $t\bar{t}$, tW and W+jet backgrounds, respectively. The variation of the luminosity and it's effect on pile-up was not taken into account.

7 Discovery potential

Table 13 shows the number of signal+background events and the number of background events for 30 fb^{-1} with the five Higgs boson masses. The statistical significance is calculated according to Poisson statistics with the program ScPf [30] which allows the systematic uncertainties to be included in the significance determination. The Monte-Carlo uncertainty, on the level of 30% on the background numbers, is not included in the significance calculation.

Table 13: Selected mass window, number of signal+background events and and number of background events for 30 fb^{-1} and statistical significance calculated with Poisson statistics. The uncertainties on the event numbers are due to the MC statistics.

	$\Delta m_{\tau^+\tau^-}$	N_S+N_B	N_B	$\Delta N_B^{syst} = 0\%$	$\Delta N_B^{syst} > 0\%$
m_A = 130 GeV/c^2, tanβ = 20	120 - 200 GeV/c^2	176	83	8.9	6.4
m_A = 140 GeV/c^2, tanβ = 15	130 - 220 GeV/c^2	136	76	9.1	6.7
m_A = 200 GeV/c^2, tanβ = 20	140 - 280 GeV/c^2	175	83	8.8	6.3
m_A = 300 GeV/c^2, tanβ = 20	240 - 480 GeV/c^2	78	39	5.4	4.3
m_A = 500 GeV/c^2, tanβ = 50	360 - 780 GeV/c^2	57	22	6.2	5.3

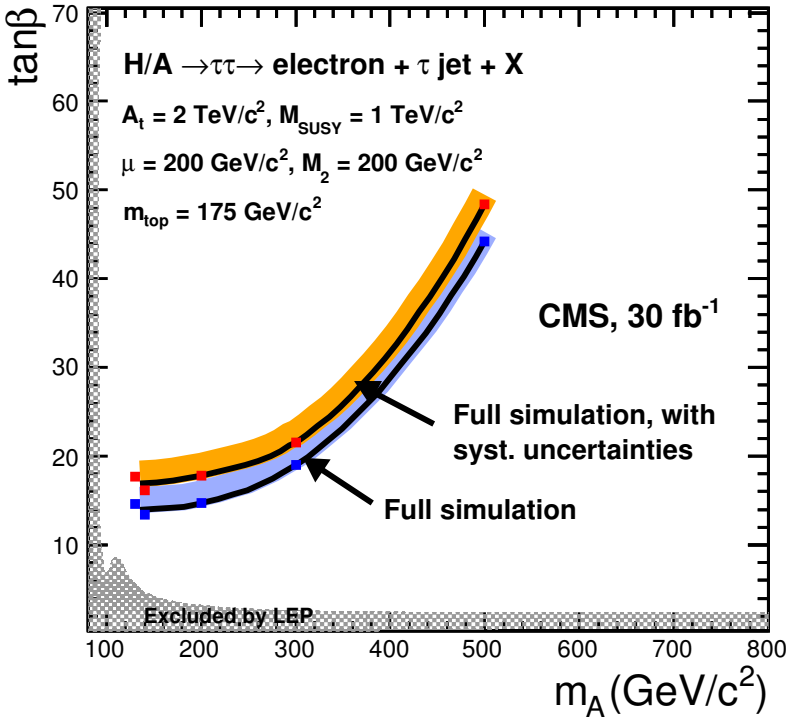

Figure 19: The 5σ-discovery potential for $\mathrm{H/A} \to \tau^+\tau^- \to$ e + jet + X for 30 fb^{-1} with maximal stop mixing. The result is shown with and without systematic uncertainties. The fast simulation result [1] for the combined electron+muon final state is also shown in the figure.

Figure 19 shows the resulting 5σ-discovery potential for $\mathrm{H/A} \to \tau^+\tau^- \to$ e + jet + X as a function of $\mathrm{m_A}$ and tanβ for 30 fb^{-1} with maximal stop mixing and μ = 200 GeV/c^2.

The other component of the lepton+jet final states, the $\mathrm{H/A} \to \tau^+\tau^- \to \mu$ + jet + X channel, has been investigated in Ref. [31]. A discovery reach extending to tan$\beta \sim 13$ around $\mathrm{m_A} \sim 200$ GeV/c^2 has been obtained. This larger discovery potential with the muon+jet final state is due to two main sources, the differences in the electron and muon identification and thresholds and the differences in the backgrounds. The trigger threshold for a single electron is 26 GeV/c, while muons with $\mathrm{p_T} >$ 15 GeV/c can be used in the single muon trigger. An identified electron was found in about 80% of the signal events while all reconstructed muons inside the fiducial volume can be exploited. An electron can pass the τ-jet trigger and the offline τ-identification cuts. Therefore the $\mathrm{Z}/\gamma^* \to \mathrm{e^+e^-}$ and $\mathrm{b\bar{b}Z}/\gamma^*, \mathrm{Z}/\gamma^* \to \mathrm{e^+e^-}$ events present a large background for the electron+jet final state and need stringent electron veto cuts in the τ identification. The hadronic QCD multi-jet events are another large background source, absent in the muon+jet channel, due to the possibility of the hadronic jet to fake both the electron and the τ jet. To suppress this background efficiently, significantly harder τ-isolation and leading track $\mathrm{p_T}$ and quality cuts were used than in Ref. [31]. A tight isolation cone (0.04) and a high $\mathrm{p_T}$ cut for the leading track (20 GeV/c) were selected, while in Ref. [31] an isolation cone of 0.07 has been used and the optimal value of the $\mathrm{p_T^{leading\ track}}$ cut has been found to be 10 GeV/c for the one-prong τ jets and to 20 GeV/c for the three-prong τ jets. Furthermore, an upper bound of 0.03 mm in the transverse impact parameter and a requirement of eight hits in the silicon tracker were found necessary for the leading track to suppress the backgrounds from fake τ's. The b tagging and the mass reconstruction procedures can be compared between these two final states. The track counting method with impact parameter measurement has been used in Ref. [31] while a probabilistic secondary vertex algorithm was used in this work. The results were found to be comparable for the efficiencies and mistagging rates. The collinear neutrino approximation was used for the Higgs boson mass reconstruction in both analysis with comparable results.

8 Conclusions

The CMS discovery potential for the MSSM Higgs bosons in the electron+jet final state from $\mathrm{gg} \to \mathrm{b\bar{b}H/A}$, $\mathrm{H/A} \to \tau^+\tau^-$ was studied with full CMS simulation and reconstruction, and with a single electron and with a combined electron-plus-τ-jet trigger. The electron from one of the τ's was identified with good efficiency and

high purity. The hadronic τ identification was performed in the tracker requiring a narrow and isolated jet with an energetic leading track. High quality was required for the momentum measurement of the leading track to suppress the hadronic jet backgrounds. For the suppression of the electronic τ candidates from the $\mathrm{Z}/\gamma^* \to \mathrm{e}^+\mathrm{e}^-$ and $\mathrm{b\bar{b}Z}/\gamma^*, \mathrm{Z}/\gamma^* \to \mathrm{e}^+\mathrm{e}^-$ backgrounds, a large energy deposition in the hadron calorimeter was required. For tagging the associated b jets a probabilistic secondary vertex algorithm was used. For further suppression of backgrounds, veto on additional central jets and an upper bound on the transverse mass reconstructed from the electron and the τ jet was used. Higgs boson mass was reconstructed exploiting the collinear neutrino approximation. Systematic uncertainties were estimated assuming that the cross sections for the $\mathrm{t\bar{t}}$ and Z/γ^* backgrounds will be measured in CMS combining several final states. After all selection cuts, the $\mathrm{b\bar{b}Z}/\gamma^*, \mathrm{Z}/\gamma^* \to \mathrm{e}^+\mathrm{e}^-$ backgrounds remain the main background components under the signal peak.

9 Acknowledgments

The authors would like to thank A. Nikitenko, I. Tomalin and W.D. Schlatter for interesting discussions and help needed to complete this work.

References

[1] S. Abdullin, S. Banerjee, L. Bellucci, C. Charlot, D. Denegri, M. Dittmar, V. Drollinger, M. Dubinin, M. Dzelalija, D. Green, I. Iashvili, V. Ilyin, R. Kinnunen, S. Kunori, K. Lassila-Perini, S. Lehti, K. Mazumdar, F. Moortgat, T. Muller, A. Nikitenko, I. Puljak, P. Salmi, C. Seez, S. Slabospitsky, S. Stepanov, R. Vidal, W. Wu, H. Yildez, and M. Zeyrek, *CMS Note 2003/006*.

[2] S. Lehti, *CMS Note 2002/035*.

[3] R. Kinnunen and A. Nikitenko, *CMS Note 1997/106*.

[4] A. Nikitenko and R. Kinnunen, *CMS Note 2003/006*.

[5] C. W. M. Carena, S. Heynemeyer and G. Weiglein, *Eur. Phys. J* **C45** (2006) 797–814.

[6] ALEPH, DELPHI, L3 and OPAL Collaborations, `hep-ex/0602042`.

[7] S. Heinemeyer, G. Weiglein, and W. Hollik, *Comput.Phys.Commun.124:76-89,2000,hep-ph/9812320; Eur.Phys.J.C9:343-366,1999,hep-ph/9812472;Site located at http://www.feynhiggs.de*.

[8] T. Sjostrand, L. Lonnblad, S. Mrenna, and P. Skands, *LU TP* **03-38** (2003) [`hep-ph/0308153`].

[9] S. Jadach, Z. Was, R. Decker, and J. Kuhn, *Comp. Phys. Commun.* **76** (1993) 361.

[10] J. Campbell, *Private communication*.

[11] *MCFM - Monte Carlo for FeMtobarn processes. Site located at http://mcfm.fnal.gov*.

[12] A. Pukhov, E. Boos, M. Dubinin, V. Edneral, V. Ilyin, D. Kovalenko, A. Kryukov, V. Savrin, S. Shichanin, and A. Semenov, *INP-MSU 98-41/542* [`hep-ph/9908288`].

[13] S. Slabospitsky and L. Sonnenschein, *Comput. Phys. Commun.* **148** (2002) 87, [`hep-ph/0201292`].

[14] V. Karimaki, *Site located at http://cmsdoc.cern.ch/cmsim/cmsim.html*.

[15] *OSCAR: Object oriented Simulation for CMS Analysis and Reconstruction, Site located at http://cmsdoc.cern.ch/oscar/.*

[16] *ORCA: CMS Reconstruction Package. Site located at http://cmsdoc.cern.ch/orca*.

[17] *CERN/LHCC 2006-001* **CMS TDR 8.1** (2006).

[18] *CERN/LHCC 2000-038* **CMS TDR 6.1** (2000).

[19] *CERN/LHCC 2002-26* **CMS TDR 6.2** (2002).

[20] G. Davattz, M. Dittmar, and A.-S. Giolo-Nicollerat, *CMS NOTE-2006/047*.

[21] G. Bagliesi et al, *CMS Note 2006/028*.

[22] C. Weiser, *CMS Note 2006/014*.

[23] G. Daskalakis, *Private communication*.

[24] Agostino, L and Pieri, M, *CMS Note 2006/078*.

[25] Voutilainen, M and Lassila-Perini, K, *CMS Note 2004/004*.

[26] Gennai, S and Nikitenko, A and Wendland, L, *CMS Note 2006/126*.

[27] M. Duhssen, `hep-ph/0303092`.

[28] S. Lehti, *CMS Note 2006/099*.

[29] S. Haywood *et. al.*, `hep-ph/0003275`.

[30] S. Bityakov, S. Erofeeva, N. Krasnikov, and A. Nikitenko, *Proceedings of PhyStat 2005, September 2005, Oxford, UK*.

[31] A. Kalinowski, M. Konecki, and D. Kotlinski, *CMS Note 2006/022*.